Carbon 146 (2019) 491–502

Contents lists available at ScienceDirect

Carbon

journal homepage: www.elsevier.com/locate/carbon

Functionalized reduced graphene oxide with tunable band gap and good solubility in organic solvents

Ulises A. Méndez-Romero [a, b], Sergio A. Pérez-García [a, **], Xiaofeng Xu [b], Ergang Wang [b, ***], Liliana Licea-Jiménez [a, *]

[a] Centro de Investigación en Materiales Avanzados S.C. (CIMAV), Unidad Monterrey, Alianza Norte 202, Parque PIIT, Apodaca, N.L., ZC, 66628, Mexico
[b] Department of Chemistry and Chemical Engineering, Chalmers University of Technology, Göteborg, SE-412 96, Sweden

ARTICLE INFO

Article history:
Received 12 October 2018
Received in revised form
7 February 2019
Accepted 8 February 2019
Available online 15 February 2019

ABSTRACT

The materials intended for organic photovoltaics and organic electronics require specific properties, such as conjugation along backbones, good solubility in organic solvents and a suitable band gap. Graphene oxide holds a high indirect optical band gap of 3 eV and a hydrophilic behavior. However, based on the fact that the graphene oxide band gap is related to the C/O ratio, chemical reduction and functionalization must be performed to obtain the proper characteristics that are required for organic applications. Here an efficient approach for chemically modified graphene oxide as a low-cost alternative for organic semiconductor materials was developed. The two synthesized materials (functionalized reduced graphene oxide and functionalized reduced graphene oxide decorated with silver nanoparticles) exhibited a 65% and 52% band gap decrease respectively, compared to graphene oxide. Moreover, both materials were soluble in organic solvents at high concentrations [10 mg mL^{-1}], turning them suitable for many applications, including organic electronics, with the additional advantage of being a solution process avoiding restacking of layers.

1. Introduction

Graphene, a single layer of carbon atoms bonded in a hexagonal array with sp^2 hybridization, exhibits a large number of outstanding characteristics, making it one of the most promising two-dimensional (2D) materials [1]. The properties of 2D materials result from the quantum confinement effects along the z-axis, leading to unusual electronic and surface characteristics. For instance, graphene possesses high optical transmittance (>97% from 400 to 1000 nm), thermal conductivity (~5000 $Wm^{-1}K^{-1}$), Young's modulus (~1.0 TPa), large specific surface area (2630 m^2g^{-1}) and extraordinary carrier mobility (2.5×10^5 $cm^2V^{-1}s^{-1}$), attributed -besides of quantum confinement-to the interaction of electrons with the periodic potential of graphene's honeycomb lattice. In this way, the particular crystalline structure (sp^2 domain) gives rise to relativistic massless Dirac fermion behavior of electrons that obey Dirac's equation instead of the Schrödinger's equation [1–7].

Moreover, graphene is a zero-band-gap material due to its π-band (bonding π molecular orbital) and π*-band (antibonding π* molecular orbital), having a characteristic shape of Dirac cones touching at the Dirac points [8]. Hence, most attention is focused on graphene applications for transparent and flexible electrodes [1]. Nevertheless, certain applications, such as organic semiconductors and organic photovoltaics (OPV), require particular properties: specific band-gap (Eg), highest occupied molecular orbital (HOMO) and lowest unoccupied molecular orbital (LUMO) energy levels, and good solubility in organic solvents as well as a low cost [9–11], which graphene can achieve only when subjected to certain chemical modifications.

Graphene oxide (GO) is the most studied graphene derivative. It basically is graphene with oxygen functional groups: hydroxyl, carboxyl, epoxy and carbonyl. GO exhibits a wide optical band gap (E_g^{opt}) of 3 eV and, therefore, a HOMO and LUMO levels [12]. The poor solubility in organic solvents, mismatching energy levels, large E_g as well as high electrical resistance [13] (~10^{11} Ω) due to the loss of crystallinity in GO, limit its applications in organic electronics.

Some of the GO challenges are to tailor the proper set of energy

* Corresponding author.
** Corresponding author.
*** Corresponding author.
E-mail addresses: alfonso.perez@cimav.edu.mx (S.A. Pérez-García), ergang@chalmers.se (E. Wang), liliana.licea@cimav.edu.mx (L. Licea-Jiménez).

https://doi.org/10.1016/j.carbon.2019.02.023
0008-6223/

levels, to improve the conductivity, to be soluble in organic solvents, and to reduce the band gap. The previous enables its use instead of common organic semiconductors in OPVs, e.g. fullerene derivatives, which present wide limitations such as low absorption, morphological instability, and high costs. In the end, these restraints generate a strong requirement to develop new semiconducting materials.

Since sp^2 domains and E_g in GO are related to C/O ratio, a promising strategy will be to reduce the amount of oxygen by chemical reduction reactions [14–16], which leads to reduced graphene oxide (rGO) with a narrower E_g and therefore, higher conductivity (~7.5×10^4 S m^{-1}) [5,12,17,18]. These chemical reactions are carried out with harmful compounds like $NaBH_4$ [14], N_2H_4 [15] and also with innocuous fructose in aqueous dispersions [16], with the inconvenience of re-stacking of the layers, which results in poor solubility.

Furthermore, common semiconducting polymers and small molecules used for OPV are soluble in organic solvents like 1,2-dichlorobenzene (*o*DCB), toluene and chloroform, in order to be processed from solution. The nature of GO is hydrophilic, but rGO has a re-dispersibility problem in polar and non-polar solvents. As a result of the chemical reduction reactions, some segments of the GO molecules recover their sp^2 domains [16], leading to a hydrophobic behavior. Thus, rGO's aggregates are difficult to dissolve or disperse in organic solvents due to the remaining oxygen groups [7]. To overcome this situation, it is critical to include chemical functionalization to increase the solubility of the material; otherwise, it is difficult to incorporate rGO into a semiconductor polymer matrix [14,19].

Previous work related to the use of graphene derivatives in OPV mainly focuses on graphene as the hole transporting layer (HTL), the electron transporting layer (ETL) and the active layers, showing satisfactory results [9,20–25]. Additionally, several reports discuss the application of graphene derivatives with metallic nanoparticles, taking advantage of the localized surface plasmon resonance, increasing the light scattering degree and thus, promoting the absorption of photons leading to a photocurrent enhancement of the final device [26–29].

Herein, we report a simple approach to synthesizing rGO with modified band-gap and good solubility, suitable for potential application as low-cost semiconductors in an active layer of OPVs. We developed reduced graphene oxide, functionalized with octadecylamine (rGO-ODA) and reduced graphene oxide functionalized with octadecylamine and decorated with silver nanoparticles (rGO-Ag), both showing different electronic properties and good solubility in *o*DCB and toluene.

2. Experimental

2.1. Materials

Graphite nanoparticles (GNPs) from ACS materials were used as starting material. $KMnO_4$, KNO_3, HCl and H_2SO_4 were purchased from CTR Scientific. Ascorbic acid-6-palmitate, 1,2-dichlorobenzene, and octadecylamine were purchased from Sigma–Aldrich. Toluene was purchased from Fisher Chemicals. Ethanol, H_2O_2, and methanol were purchased from J.T. Baker. All the chemicals were used as received.

2.2. Characterization equipment

High-resolution C1s X-ray photoelectron spectroscopy (XPS) analyses were carried out using a Thermo Scientific Escalab 250Xi instrument. The base pressure during the analysis was ~10^{-10} mbar and the photoelectrons were generated with the AlKα (1486.68 eV) X-ray source, using monochromator, and a spot size of 650 μm. The X-ray voltage and power were 14 kV and 350 W, respectively. The acquisition conditions for the high-resolution spectra were 20 eV pass energy, 45° take-off angle and 0.1 eV/step. Selected regions spectra were recorded, covering the C1s, O1s, and N1s photoelectron peaks. They were fitted using a Gaussian-Lorentzian function and a Shirley background subtraction. The recorded photoelectron peaks were curve-fitted using the Advantage software V 5.41.

A PerkinElmer FT-IR Spectrometer Frontier was used in ATR mode, from 400 to 4000 cm^{-1}. The UV–Vis–NIR Spectrometer PerkinElmer instruments Lambda 900 was used for E_g^{opt} determination. A VWR Symphony Ultrasonic Cleaner Model 97043-944 was used. An Electrochemical Workstation CH-Instruments 650A was used for HOMO-LUMO determination. The Scanning Electron Microscopy FEI Nova NanoSem200 in STEM mode was used for morphology characterization. The X-ray diffractometer Panalytical Empyrean was used for interplanar distance determination. An inductively coupled plasma-atomic emission spectroscopy Thermo Electron-ICAP 6500 was used for transfer efficiency. A Profilometer Tencor D-100 KLA was used to analyze the roughness of the films. The Dynamic Light Scattering (DLS) Malvern Zetasizer Nano S was used to determine the size distribution.

2.3. Method

We started from GNPs (see SI Fig. S1), working with modified Hummers' method reported elsewhere [16,30,31]. The obtained GO aqueous dispersion resulted with an E_g^{opt} of 3 eV, see SI Fig. S2. After that, a phase-transfer from water to a desired organic solvent was performed to achieve an electrostatically functionalized GO with octadecylamine (GO-ODA). In order to synthesize rGO-Ag, as a second approach, a solution of Ag^+-ODA was prepared and mixed in the same solvent for GO-ODA. Finally, an *in situ* chemical reduction was carried out with ascorbic acid-6-palmitate for both dispersions, GO-ODA and the mixture of GO-ODA/Ag^+-ODA, obtaining rGO-ODA and rGO-Ag.

2.4. Graphene oxide synthesis

The GO synthesis was carried out from GNPs by a modified Hummers' method [16,30]: 0.5 g of GNPs were oxidized in 30 mL of H_2SO_4 and 0.295 g of KNO_3 with 3 g of $KMnO_4$ to achieve formation of Mn_2O_7 complex. The reaction was set for 6 h, stirring at 450 rpm controlling the temperature below 15 °C. It was quenched with 100 mL of DI H_2O and 6 mL of H_2O_2 30%. Next, the obtained bright yellow dispersion (graphite oxide) was centrifuged at 3500 rpm for 10 min, to remove the supernatant. 100 mL of HCl 10% were added to the precipitate and centrifuged under the same conditions. The washing process was repeated 3 times with DI H_2O. Thereafter, 80 mL of DI H_2O were added and the dispersion was placed in the ultrasonic bath for 1 h for exfoliation, followed by centrifugation at 3500 rpm for another hour. Finally, the supernatant (GO as water dispersion) was recovered and stored. Fig. 1 schematically depicts the described reaction.

2.5. Functionalization

The functionalization of the fresh synthesized GO dispersed in water, fixed at [10 mg mL^{-1}] and the $AgNO_3$ water solution [4×10^{-3} M] to *o*DCB or toluene was performed electrostatically, by mixing a solution of ODA in ethanol [30 mg mL^{-1}] in a 1:1 vol ratio and sonicated for 5 min. In both cases, the mixture was stirred at 450 rpm for 5 min at room temperature. Subsequently, an equal volume of the desired solvent (*o*DCB or toluene) was added and stirred at 450 rpm for 3 min at room temperature, promoting a

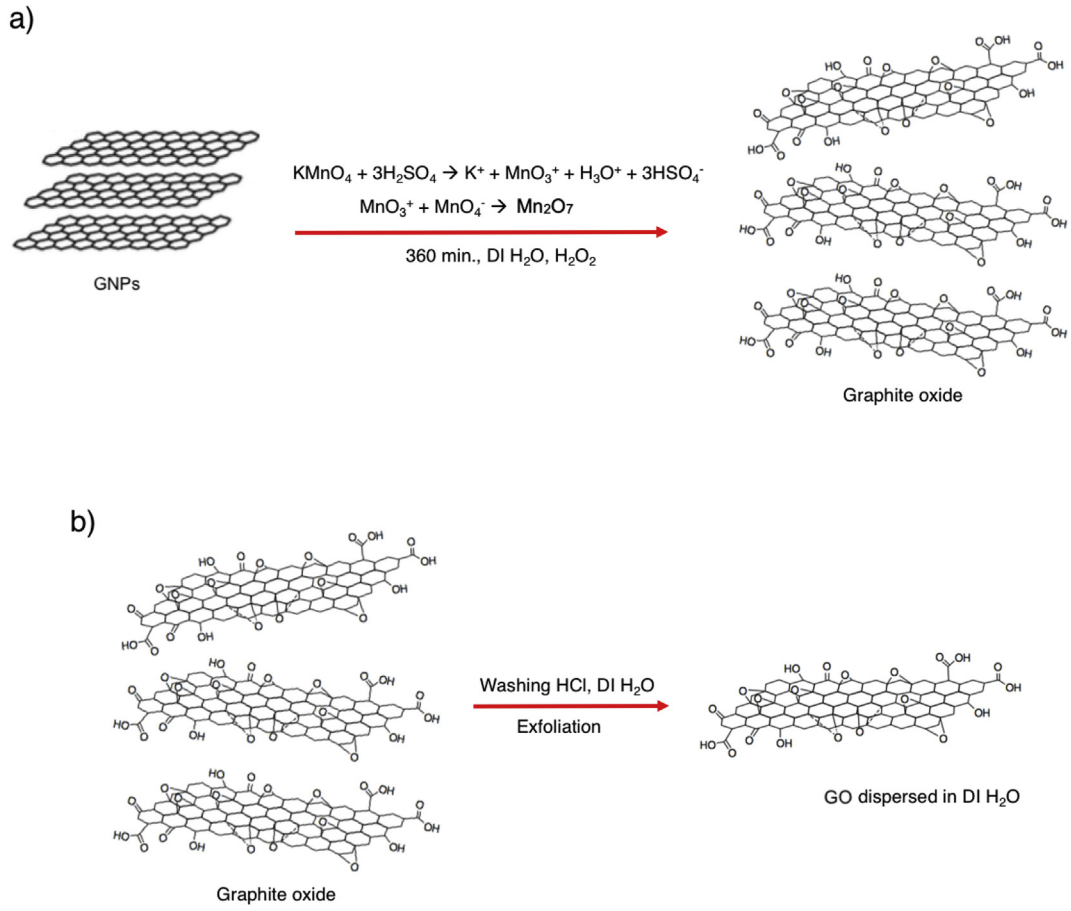

Fig. 1. Graphene oxide synthesis. a) Modified Hummer's method to obtain graphite oxide from graphite nanoparticles. b) GO's water dispersion after washing by centrifuge and exfoliation. (A colour version of this figure can be viewed online.)

phase transfer (see SI Fig. S3). The organic phases (GO-ODA and Ag^{+}-ODA) were stored for later use. The silver transfer efficiency was calculated by ICP analysis, yielding 97.2% efficiency. Finally, GO-ODA and Ag^{+}-ODA were mixed and stirred at 450 rpm for 20 min at room temperature. In Fig. 2, we show a schematic diagram representing this process. Compared with a previous report using alkylamines [14], here we demonstrate the versatility, easy method and lower molar concentration required for a complete phase

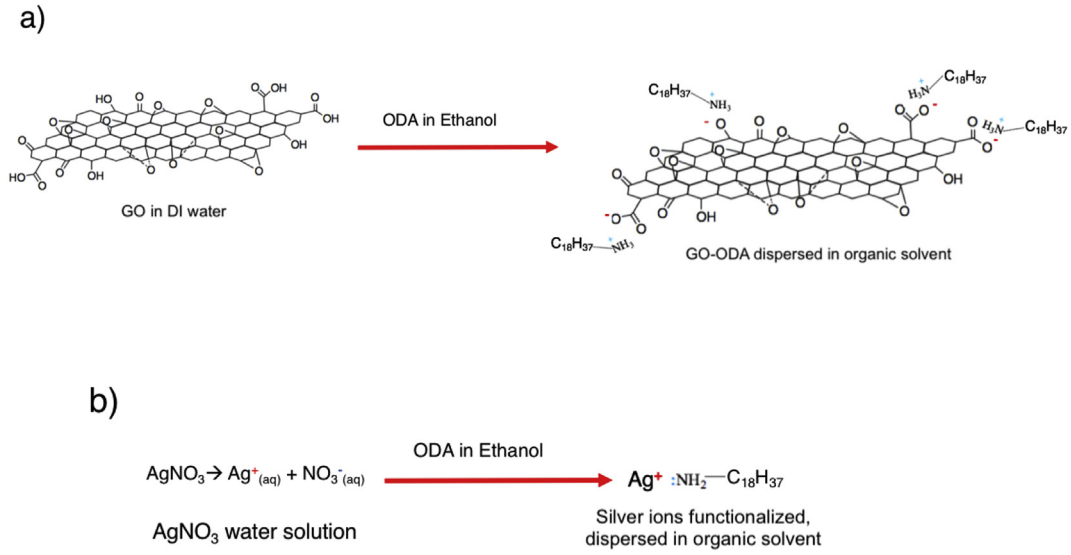

Fig. 2. Electrostatic functionalization by ODA. a) GO dispersed in water and functionalized by ODA and transferred to *o*DCB or toluene. b) Functionalization of silver ions by ODA and transferred to *o*DCB or toluene. (A colour version of this figure can be viewed online.)

transfer by an electrostatic functionalization. After chemical reduction, functionalization will become covalent, avoiding the use of harmful coupling agents like N,N′-dicyclohexylcarbodiimide (DCC) [32].

2.6. Chemical reduction

The chemical reduction reactions were carried out by adding 100 μL of ascorbic acid-6-palmitate (AA6P) [100 mM] solution in *o*DCB or toluene for each 100 mg of GO, at 98 °C and stirred at 450 rpm for 2 h. Thus, reduced graphene oxide functionalized with ODA (rGO-ODA) and reduced graphene oxide functionalized with ODA and decorated with silver nanoparticles (rGO-Ag) were obtained in solution (see SI Fig. S4). Both samples were vacuum filtered in a Pall PTFE membrane with a diameter of 47 mm and 0.2 μm pores and dried at room temperature for further characterization. The proposed mechanism of the chemical reduction reaction is described below in Fig. 3 for rGO-ODA and rGO-Ag. In summary, the ascorbic acid-6-palmitate reduces the epoxy groups, while the carboxyl and carbonyl are thermally reduced. Because carboxyl is electrostatically bonded to the amine, the reaction allows a condensation, creating a covalent bonding with water as a by-product, which eventually evaporates from the reaction media [7,15].

3. Results and discussion

As discussed above, some of the main drivers for a successful material to be used as a semiconductor rely on the nature of the chemical modifications that take place within the system. In order to understand the chemical behavior and modifications of the graphene-based material at its surface, ATR-FTIR and XPS measurements were performed.

Nevertheless, as the chemical reduction decreased the C/O ratio, the resulting materials had smaller E_g, which was analyzed by UV–Vis–NIR and cyclic voltammetry (CV) for the optical (by Tauc

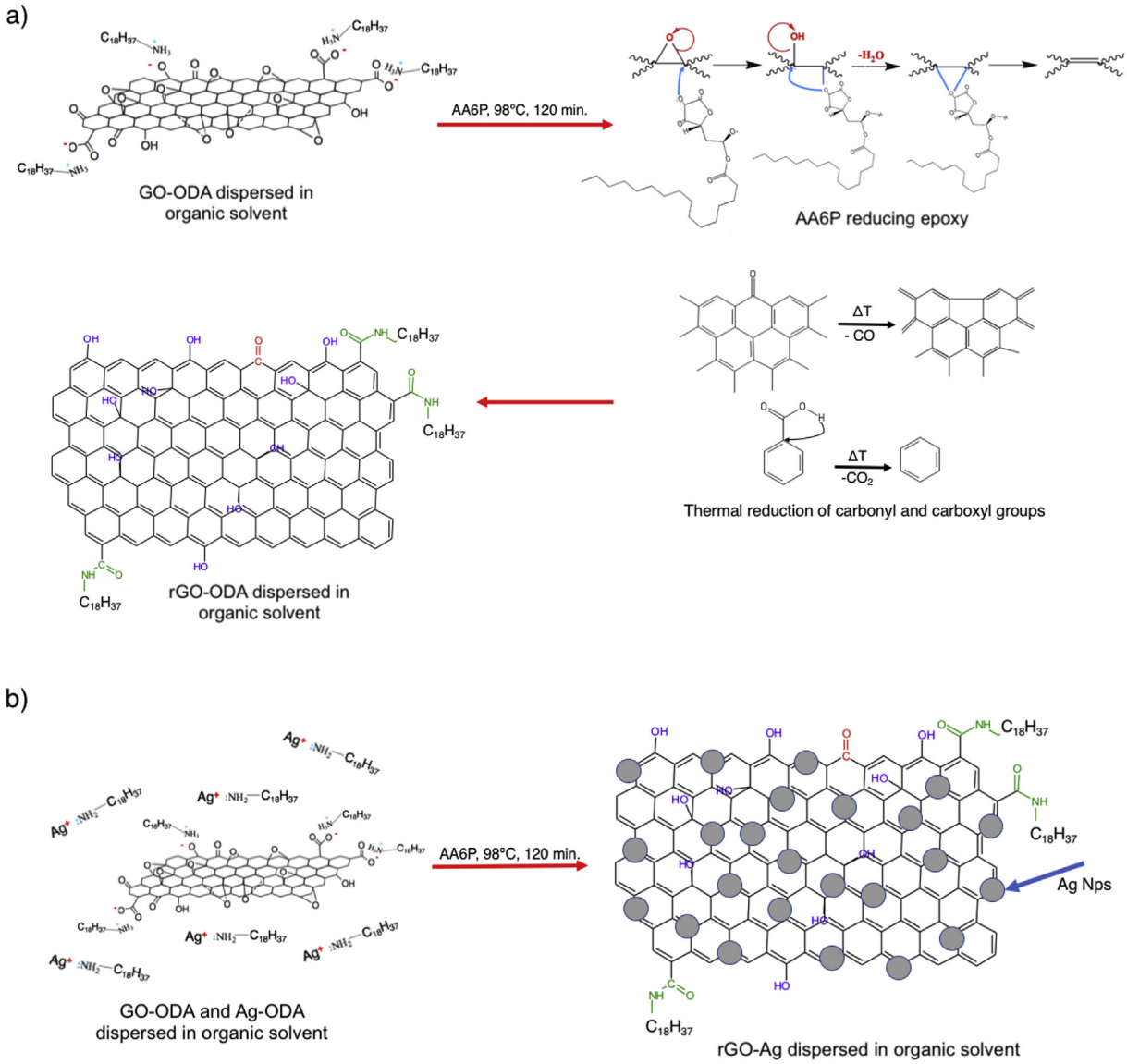

Fig. 3. Proposed mechanism for the chemical reduction. a) Chemical and thermal reduction of graphene oxide functionalized to generate reduced graphene oxide functionalized (rGO-ODA). b) Chemical and thermal reduction for the mixture of functionalized graphene oxide and functionalized silver ions, in order to obtain functionalized reduced graphene oxide decorated with silver nanoparticles (rGO-Ag). (A colour version of this figure can be viewed online.)

plots) and electrical band-gaps, respectively. Also, the morphology and size of the graphene oxide synthesized and used in the present work were studied by SEM in STEM mode to measure the lateral dimension, and analyzed by DLS for statistical purposes. Finally, to analyze the behavior of the synthesized materials into the nanocomposite, the roughness and UV–Vis absorption of a polymer:-rGOs films were carried out.

3.1. Analysis of chemical modifications obtained during the synthesis

To investigate the chemical structures of the synthesized materials, an ATR-FTIR analysis was performed. In order to tell apart the original GO and the rGOs, the common peaks of oxygen functional groups are presented in Fig. 4. For instance, the GO spectrum (red line, 1) presents various oxygen functional groups: the typical broadband from 3000 cm^{-1} to 3700 cm^{-1} pointed at 3200 cm^{-1} that refer to ν_1 hydroxyl (OH), ν_1 carbonyl (C=O) at 1719 cm^{-1}, ν_1 aromatic (C=C) at 1618 cm^{-1}, ν_1 alkoxy (C–O) at 1160 cm^{-1} and ν_1 epoxy (C–O–C) at 1030 cm^{-1}. All features corresponding to highly-oxidized graphene oxide, according to previous reports [33–35].

For rGO-ODA and rGO-Ag, the prominent ν_1 hydroxyl band is completely removed, as well as the ν_1 carbonyl. On the other hand, the most perceptible bands for both are at 2915 cm^{-1} and 2850 cm^{-1} corresponding to ν_3 and ν_1 of C–H, respectively [36], confirming a complete chemical reduction process. Furthermore, the ν_1 and ν_2 vibrations of carbon-nitrogen bonding in the amine (C–NH–C) at 3444 cm^{-1} and at 1560 cm^{-1}, also the ν_1 for NH is recorded at 1470 cm^{-1} [37,38]. The ν_1 for C–O and C–O–C at 1150 cm^{-1} and 1070 cm^{-1} present a small shift from the GO original positions [39]. Finally, the ν_3 and ν_1 for N–O bonding can be observed at 718 cm^{-1} and 618 cm^{-1}, respectively [36], suggesting that besides the reduction, the functionalization takes place with the carboxylic and hydroxyl groups as proposed in Fig. 2. On the other hand, the transmittance of rGO-ODA and rGO-Ag is high, revealing the lower restacking level due to the synthesis method used in this work.

Furthermore, for a deeper analysis of the surface chemical state, the synthesized materials were analyzed by X-ray photoelectron spectroscopy (XPS). The C1s core level spectra are shown in Fig. 5, GNPs Fig. 5a) for the raw material, GO Fig. 5b), rGO-ODA Fig. 5c), rGO-Ag Fig. 5d). The high-resolution C1s spectra were recorded from 279 eV to 298 eV. The signal coming from the initial material (GNPs) is composed only by C–C and C=C, with a single contribution at 284.48 eV without any degree of oxidation in accordance to the ATR-FTIR results confirmed by XRD, both in SI Fig. S1 c) and d). After the oxidation of the GNPs by the Hummers' reaction, the C1s signal matches not only with C–C and C=C but, also C–O and C=O at 286.88 eV and 288.88 eV, respectively [16,40], in agreement with the ATR-FTIR results shown in Fig. 4.

Finally, the signals coming from both rGO-ODA and rGO-Ag are characteristic of a highly reduced state, presenting a very small contribution of C–O at 288.08 eV and a new signal related to C–N at 285.48 eV, suggesting a covalent functionalization by ODA [41]. This result is in accordance with the ATR-FTIR spectra in Fig. 4.

From the XPS results, we calculated the C/O ratio for each material from the high-resolution C1s, as well as the surface elemental composition. Also, the optical band gap obtained from UV–Vis–NIR (explained in sec. 3.2) is depicted in Table 1.

3.2. Optical band gap determination (E_g^{opt})

The analysis of the E_g^{opt} values by UV–Vis spectroscopy was extended to the near infrared region (UV–Vis–NIR) from 200 nm to 2100 nm. This was analyzed because the absorbance of rGO-ODA and rGO-Ag follow a different behavior when compared to GO, i.e., zero absorbance at greater wavelengths. However, this behavior could be attributed to rGOs because of the linear dispersion by Dirac's electrons [18,42,43], which is also good evidence of a highly reduced graphene oxide, with recovered sp^2 hybridization.

For measurements, filtered and dried dispersions of rGO-ODA

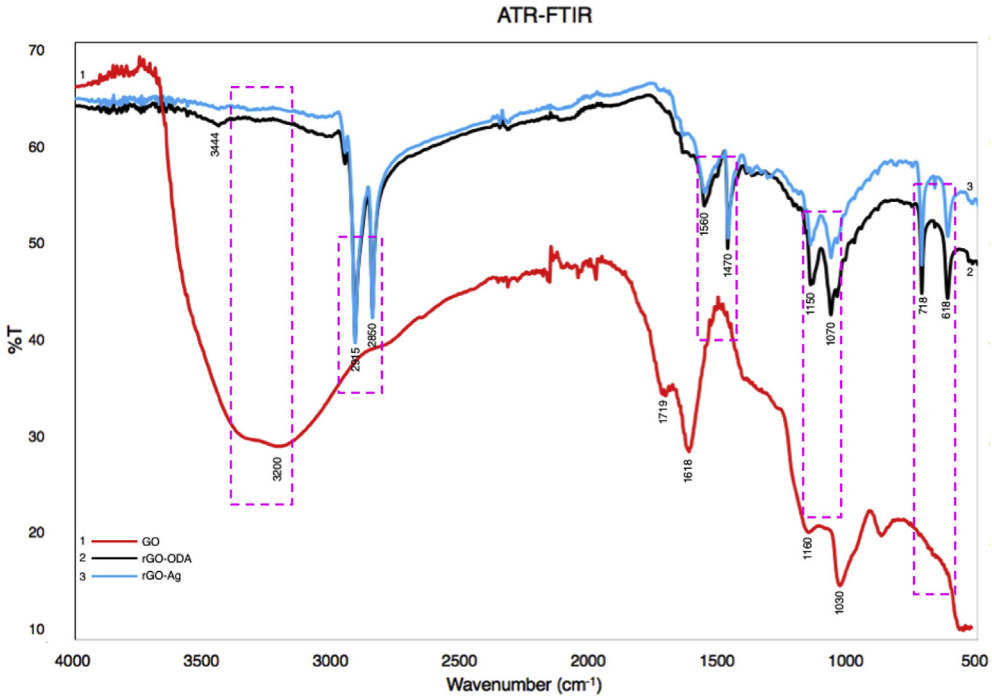

Fig. 4. ATR-FTIR spectra of GO, rGO-ODA and rGO-Ag. (A colour version of this figure can be viewed online.)

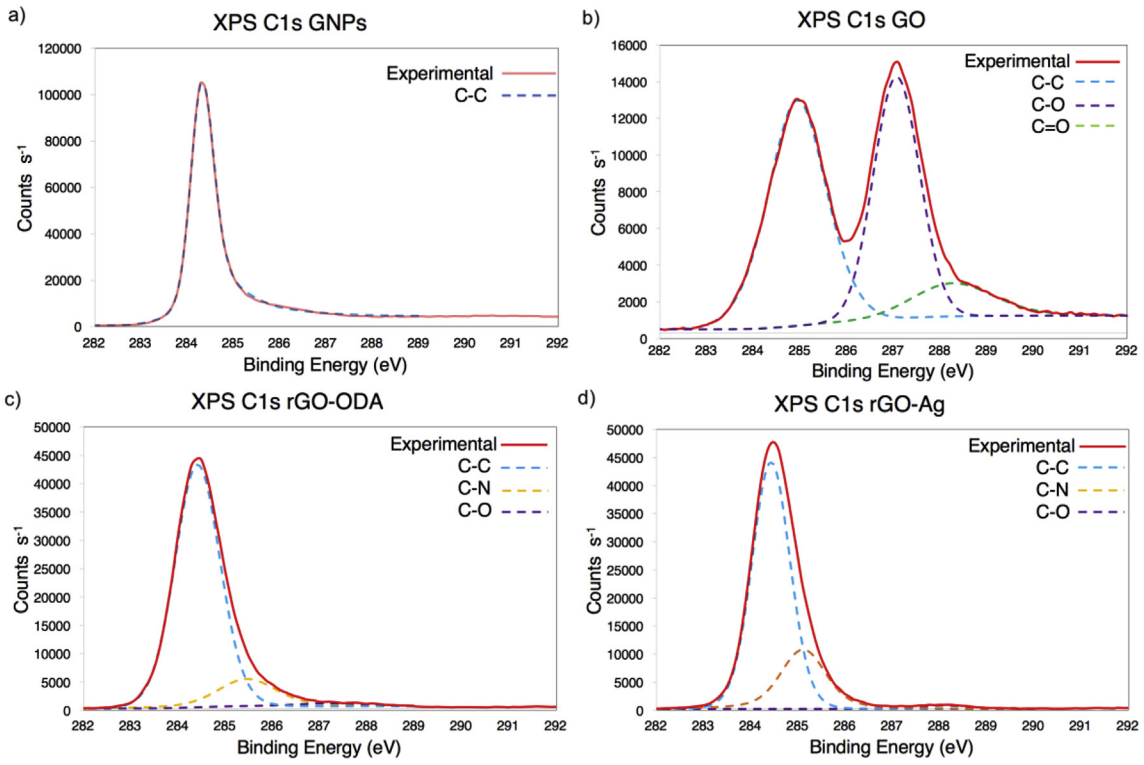

Fig. 5. High resolution XPS C1s analysis: a) GNPs, b) GO, c) rGO-ODA and d) rGO-Ag. (A colour version of this figure can be viewed online.)

Table 1
Surface elemental composition, C/O ratio and optical band gap.

Sample	C/O ratio	N Atomic %	Ag Atomic %	E_g^{opt} (eV)
GO	1.95	–	–	3
rGO-Ag	81.84	3.85	0.065	1.49
rGO-ODA	99.77	1.91	–	1.1

and rGO-Ag were carried out in acetonitrile at a concentration of 0.05 mg mL^{-1} and sonicated for 30 min. Acetonitrile was used to prepare the dispersions due to its optical transparency in the UV–Vis–NIR range, which is shown in Fig. 6 with a pink dashed line 4. Thus, the spectra measured for rGO-ODA and rGO-Ag represent only a contribution of the corresponding material.

For instance, the spectra of rGO-ODA and rGO-Ag show peaks around 255 nm and peaks at ~1400 nm and ~1900 nm, corresponding to C–N and its overtone [44]. It should be noticed that rGO-ODA presents a higher absorbance than rGO-Ag, despite the fact of being at the same concentration (0.05 mg mL^{-1}).

In order to analyze GO in UV–Vis–NIR, the exfoliation phase was performed in methanol. As one can see from Fig. 6 (dotted grey curve 5), the absorbance of methanol only influences from 200 nm to 240 nm and from 1480 nm to 1870 nm. Therefore, the regions of interest could be analyzed, observing a clear difference in absorption between rGO-ODA and rGO-Ag compared to GO, attributed to C–N peaks located at 1400 nm and 1900 nm [44].

It is difficult to determine the absorption onset and directly deduce the band-gap from it. Therefore, in order to analyze the indirect E_g^{opt} values with a more precise approach, Tauc plots were performed and are shown in Fig. 7 using the UV–Vis–NIR data. The Tauc's relation [12,45] is:

$$(\alpha h\nu)^{\frac{1}{2}} = (h\nu) - E_g \tag{1}$$

From Lambert Beer's law the coefficient (α) was obtained using the absorbance *(A)* and transmittance *(T)* (in Eqs. (2) and (3)):

$$A = -Log_{10}\frac{I}{I_0} \tag{2}$$

And

$$T = \frac{I}{I_0} = e^{-\alpha z} \tag{3}$$

It can be noticed that α is described in absorbance terms, as presented in Eq. (4), considering that the optical path *(z)* is equal to 1 cm:

$$\alpha = -Ln\left(10^{-A}\right) \tag{4}$$

After this, we only need to convert the wavelength *(λ)* into energy, using the Planck's constant *(h)* in eV units and the velocity of light *(c)* (described in Eq. (5)):

$$E = \frac{hc}{\lambda} = h\nu \tag{5}$$

Using the results calculated with Eqs. (1)–(5), we constructed the Tauc's plot to determine the E_g^{opt} value, extrapolating a tangent line (dotted) to achieve intersection with the *x* axis (E_g^{opt} in eV), as shown in Fig. 7.

As a matter of fact, after the chemical reduction -the initial E_g^{opt} of 3 eV for the GO- undergoes a considerable decrease, reaching the value of 1.1 eV for rGO-ODA and 1.49 eV for rGO-Ag. Similar results have been reported for the synthesis performed with ascorbic acid or fructose in water dispersions [16]. However, in our case, the synthesis technique has the benefit of shorter reaction time (2 h) and the final product is functionalized and is dispersed in the desired organic solvent, preventing the agglomeration. Since both

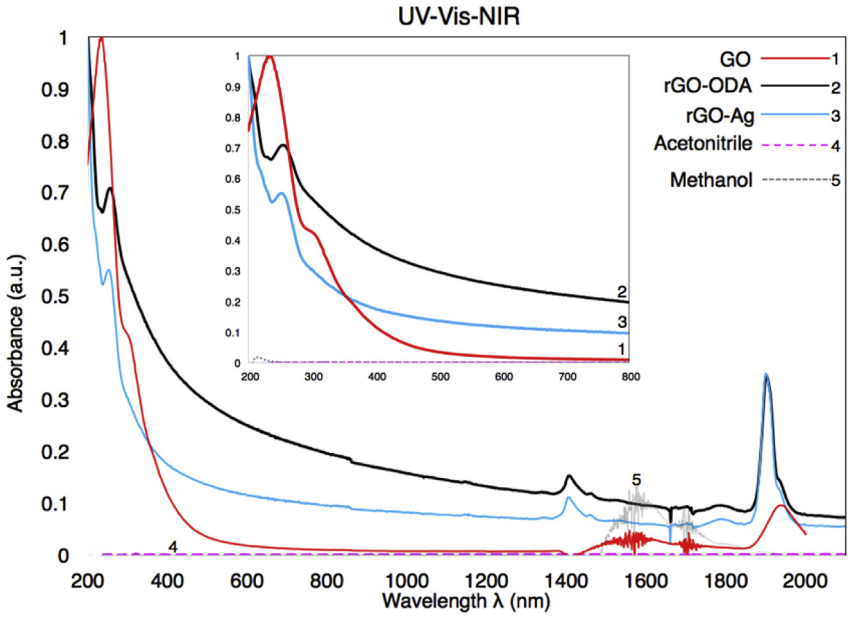

Fig. 6. UV–Vis–NIR spectra of GO, rGO-ODA, rGO-Ag, acetonitrile and methanol. (A colour version of this figure can be viewed online.)

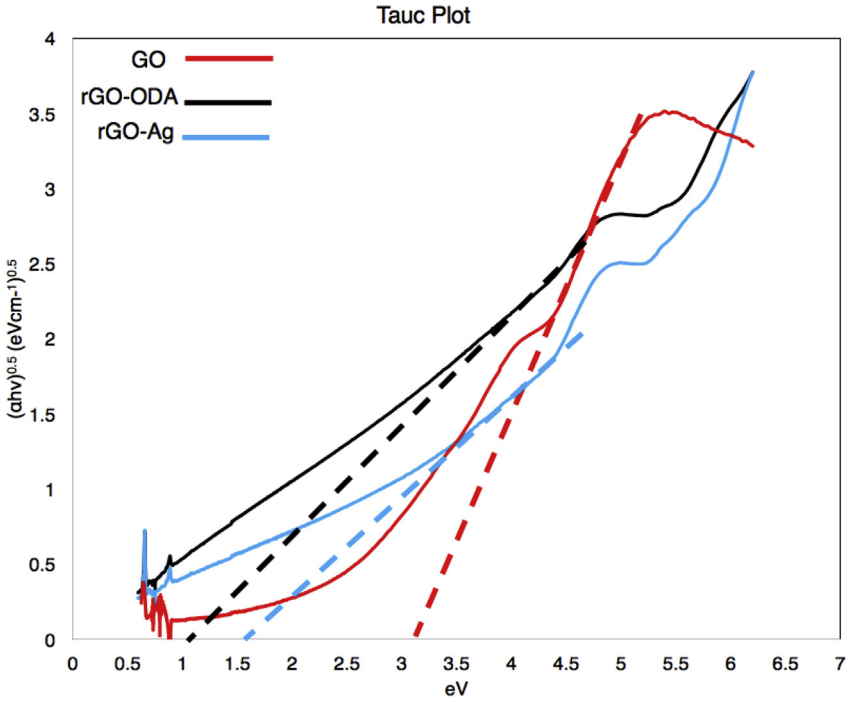

Fig. 7. Tauc's plots of GO, rGO-ODA and rGO-Ag. The extrapolation of the dotted tangent lines, intersect the x-axis, defining the E_g^{opt} accordingly with Eq. (1). (A colour version of this figure can be viewed online.)

materials were synthesized under the same conditions, the difference in E_g^{opt} values can be explained by the presence of silver ions, which were also reduced by the ascorbic acid-6-palmitate, in the case of rGO-Ag.

In addition, we present the absorption coefficient ε (Fig. 8), which was calculated by Eq. (6) using absorbance (A), concentration (c) of the rGOs and the optical pathway (b) (fixed to be 1 cm).

$$\varepsilon = \frac{A}{bc} \tag{6}$$

In Fig. 8, rGO-ODA presents a higher absorption coefficient compared to rGO-Ag. Moreover, all the rGOs exhibit strong [46,47] absorption in the ultraviolet region, showing potential applications for developing UV detectors.

3.3. HOMO-LUMO levels and electrochemical band gap (E_g^{cv})

The study of energy levels corresponding to the highest occupied molecular orbital (HOMO) and the lowest unoccupied molecular orbital (LUMO) was performed with cyclic voltammetry (see

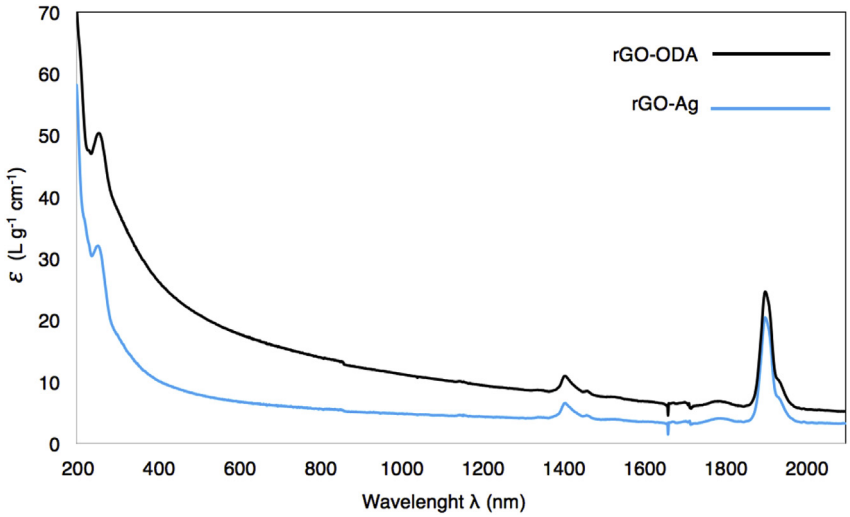

Fig. 8. Absorption coefficient of rGO-ODA and rGO-Ag from 200 nm to 21000 nm in acetonitrile dispersion. (A colour version of this figure can be viewed online.)

SI Fig. S5), using the onset oxidation and reduction values obtained from the voltammetry programs. The HOMO and LUMO values were calculated with reference against ferrocene using the following equations [11]:

$$E_{HOMO} = -(E_{ox} + 5.13)eV \quad (7)$$

$$E_{LUMO} = -(E_{red} + 5.13)eV \quad (8)$$

By definition, the electrochemical band-gap energy (E_g^{cv}) is the energy difference between HOMO and LUMO. The E_g^{cv} measured directly by cyclic voltammetry present expected discrepancies in comparison to the E_g^{opt} obtained from UV–Vis NIR data. This difference can be attributed to the intrinsic nature of the methods *per se* used for the measurements, as reported by Gedefaw, D., et al. [11] Fig. 9 illustrates the CV curves for the different materials.

The HOMO-LUMO values obtained from Equations (7) and (8) are summarized in Fig. 10. The resulting E_g^{cv} shows a decrease, being 2.54 eV for GO, 2.18 eV for rGO-Ag and 1.21 eV for rGO-ODA, in accordance to XPS results, where the decrease in oxygen content lowers the value of E_g. However, the addition of nitrogen and silver nanoparticles plays an opposite effect, complicating the accurate prediction. Fig. 10 presents the synthesized materials in comparison to materials commonly used as active layers for OPVs, including P3HT: $PC_{61}BM$ [9] (Fig. 10a) and TQ1: $PC_{71}BM$ [10,11] (Fig. 10b) as a reference. GO-ODA intermediate characteristics can be found at S5 and S6 pages in the supplementary information.

As one can see (Figs. 9 and 10), the LUMO levels of GO, rGO-ODA, and rGO-Ag are comparable to those of PCBMs that are used in OPV as acceptors [48]. Nevertheless, considering that the ideal E_g of an active OPV layer is expected to be around 1.75 eV [49] and the Shockley–Queisser limit for inorganic semiconducting materials is 1.34 eV [50], it might seem that the chemical reduction narrows the band gap markedly for rGO-ODA. However, as the E_g of graphene-based materials is related to their C/O ratio, it can be further fine-tuned to the desired value by changing the reduction parameters, the concentration of reducing agent and the degree of functionalization, as previously reported by our group [16]. Moreover, such a

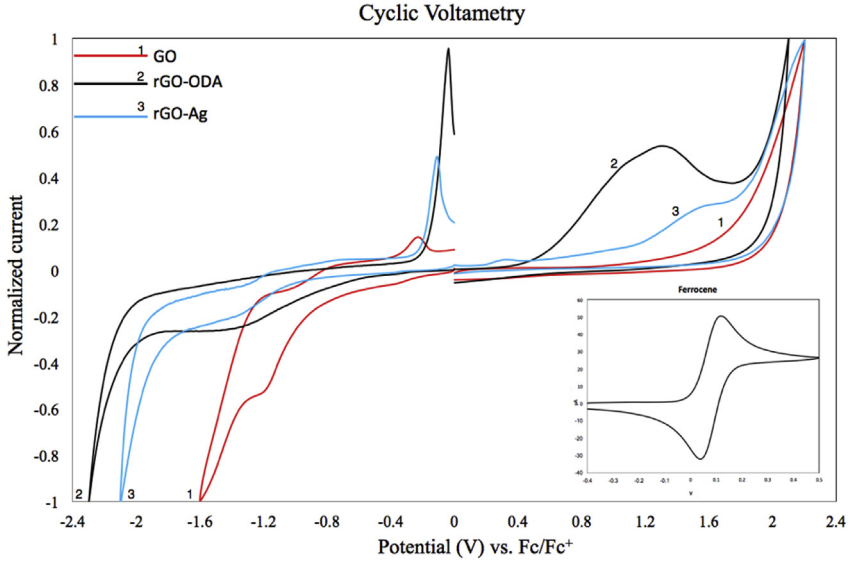

Fig. 9. GO, rGO-ODA and rGO-Ag voltamperograms. (A colour version of this figure can be viewed online.)

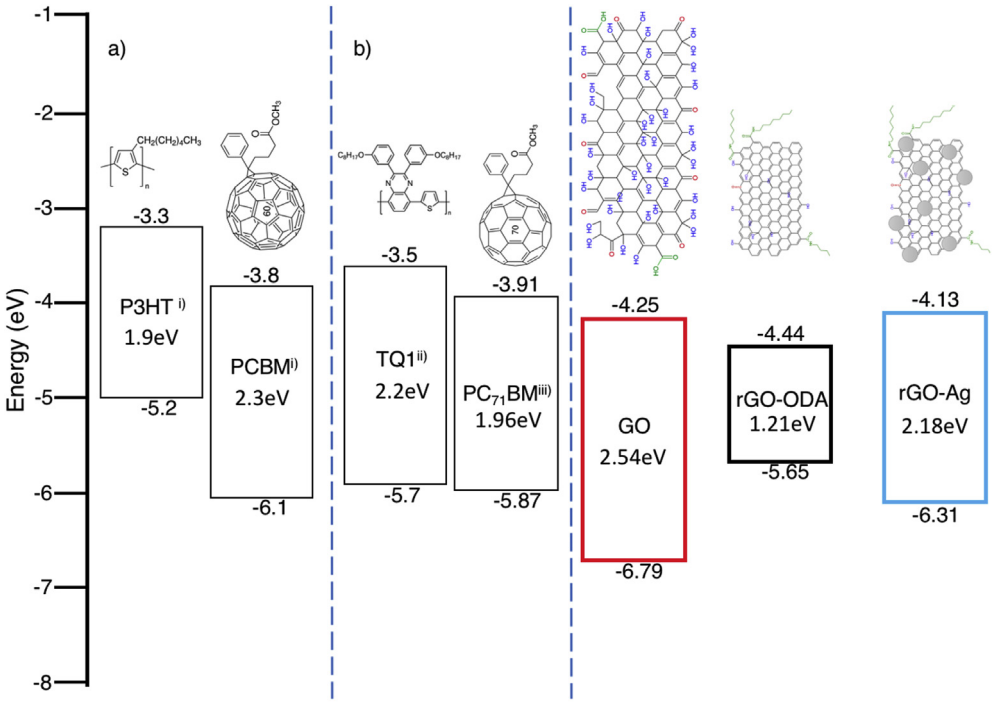

Fig. 10. Diagram summarizing HOMO-LUMO energy levels and band gap. a) P3HT:PCBM [i] [9] b) TQ1:$PC_{71}BM$ [ii] [11] [iii] [10], as well as the synthesized GO, rGO-ODA and rGO-Ag. (A colour version of this figure can be viewed online.)

low value of E_g opens a new area of study concerning the possible applications of the synthesized materials in the near infrared region, i.e., in the field of sensors and transparent PV [51].

3.4. Polymer: rGOs blending feasibility

In order to analyze the viability to incorporate rGO-ODA and rGO-Ag into the active layer of an OPV cell, absorbance tests were performed in films deposited by spin coating at 1000 rpm for 30 s. We used TQ1:rGO-ODA and TQ1:rGO-Ag dispersed in toluene with a ratio of 1:1 in [5 mg mL^{-1}]. The UV–Vis spectra of the corresponding materials are shown in Fig. 11. The spectra from the films corresponding to TQ1:rGO-ODA and TQ1:rGO-Ag present a displacement from the baseline, which is probably due to the light scattering of rGO. It is important to notice the bathochromic shift of the TQ1:rGO-ODA blend (dotted lines in Fig. 11) attributed to a synergy between the rGO and TQ1 (wider E_g), allowing to harvest a greater number of photons and, therefore, a greater exciton

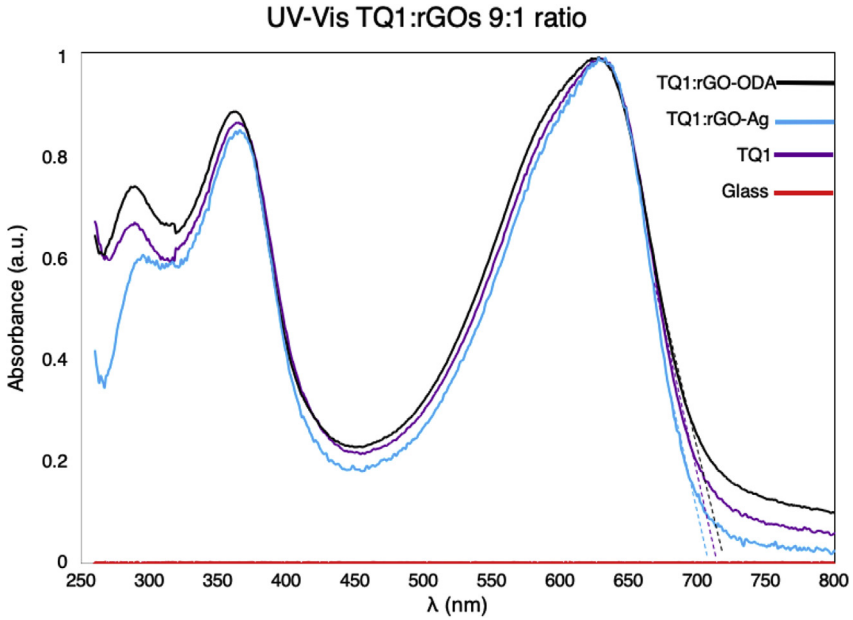

Fig. 11. UV–Vis spectra of blended films TQ1:rGOs at 9:1 ratio. (A colour version of this figure can be viewed online.)

photogeneration [52].

The quality of the films was further studied with surface roughness analysis performed by a profilometer. For comparison purposes, the roughness of the glass and pure TQ1 film were also included in Fig. 12. A higher roughness is observed for the TQ1:rGO-ODA film, and the lower one for the TQ1:rGO-Ag film. This can be explained as a result of the better solubility of rGO-Ag and a possible agglomeration for rGO-ODA. The TQ1:rGO-Ag film presents a very smooth surface, which is of particular interest for OPV and other thin film applications.

3.5. GO lateral dimensions

It is important to determine the size of rGO flakes. Therefore, SEM and DLS were performed, indicating that the average lateral dimensions for rGO-ODA and rGO-Ag were ~80 nm. Samples were studied by SEM in STEM mode, adding 5 μL of GO [0.01 mg mL^{-1}] onto a TEM grid Formvar 300 mesh Cu and drying the droplets at room temperature. The graphene oxide micrograph is shown in Fig. 13a. DLS measurements for the size distribution of graphene oxide in water dispersion were also performed, yielding a symmetric bell-shaped distribution (Fig. 13b) with an average size of 84.1 nm and a range between 20 nm and 400 nm. This concurs with the size acquired from STEM measurements.

It is important to mention that DLS is an indirect technique, measuring fluctuations on dispersions due to Brownian motion that allows calculation of the diffusion coefficient, using the Stokes-Einstein equation, providing the particles' size in dispersion that is considered to have spherical geometry [53]. Therefore, this approach rarely applies to graphene-like materials. Although, some publications describe the GO in aqueous dispersion as a spherical structure, depending on the values of pH and zeta potential conditions [54–56], which is correlated to the results reached by STEM.

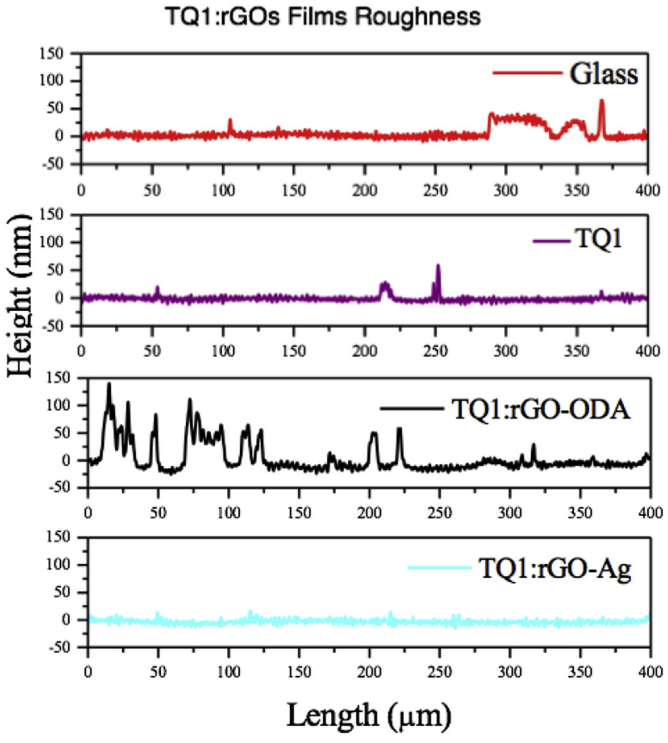

Fig. 12. Roughness analysis of blended films of TQ1:rGOs. (A colour version of this figure can be viewed online.)

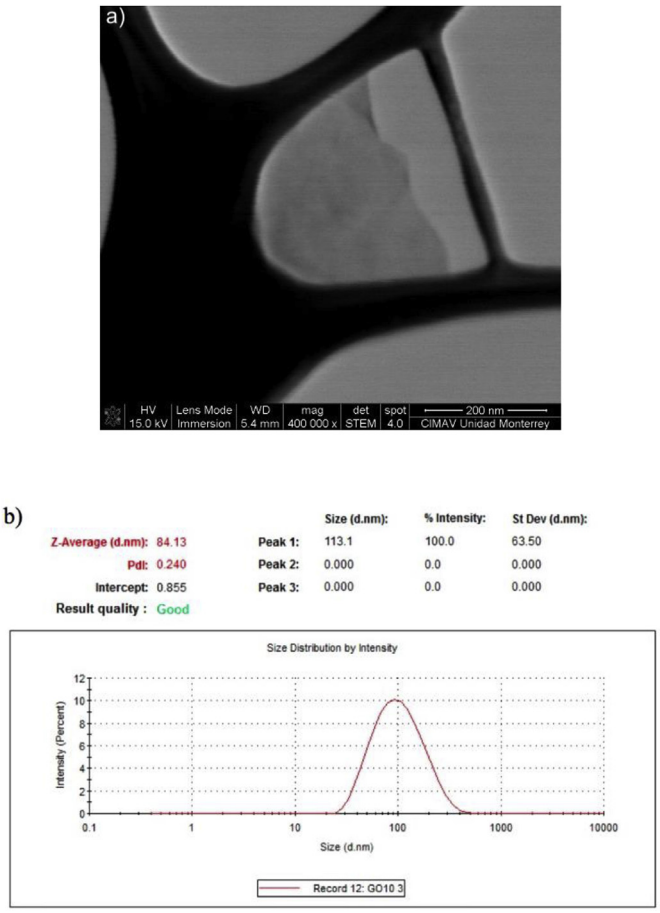

Fig. 13. Size of graphene oxide particles. a) STEM image of GO and b) Size distribution of GO by DLS. (A colour version of this figure can be viewed online.)

From these results, we can conclude that our method for synthesizing different functionalized GOs yields the bandgap value E_g comparable to the commonly used PCBM acceptors in OPVs. The synthesized rGOs feature good solubility in non-polar solvents such as toluene, *o*DCB with concentration up to 10 mg mL^{-1} and 5 mg mL^{-1} in chloroform. And for GO, in polar solvents like water and methanol, which enables its use in OPVs and organic electronics as well.

4. Conclusions

Organic semiconductor materials based on graphene oxide with controlled E_g and good solubility in organic solvents were developed. Additionally, this process allows circumventing the restacking of the layers and stability problems, as the whole process was carried out in solution. Thus, the van der Waals forces and π-π interactions of the layers were overcome. The simplicity of the functionalization, eco-friendly chemical reduction and low-cost of the initial material compared with PCBMs, are some of the main benefits that open an area for improvement for the synthesis of rGO as a promising candidate for various applications. Because these graphene-based materials have an absorbance in the UV–Vis region, they can be used from OPVs to other organic electronics, such as sensors, OLEDs, and photodetectors. Moreover, the HOMO and LUMO levels measured for GO, rGO-ODA, and rGO-Ag reported in this study will be useful for OPV application and may also inspire the community to explore other potential applications.

Acknowledgements

Authors are grateful for the technical support and facilities at CIMAV Campus Monterrey and Chalmers University of Technology, Department of Chemistry and Chemical Engineering, as well as the Mexican National Research Council CONACyT (México) for the scholarship and Network of nanosciences and nanotechnology RedNyN (México) for the financial support (Ulises Méndez.).

We would also like to thank the technical staff of CIMAV Campus Monterrey: Lilia Magdalena Bautista Carrillo for ATR-FTIR, DLS and zeta potential measurements; Luis Gerardo Silva Vidaurri for XPS measurements; and Nayely Pineda Aguilar for SEM micrographs. Ergang Wang acknowledges the Swedish Research Council VR (Sweden) and Formas (Sweden) for financial support.

Appendix A. Supplementary data

Supplementary data to this article can be found online at https://doi.org/10.1016/j.carbon.2019.02.023.

References

[1] R. Garg, S. Elmas, T. Nann, M.R. Andersson, Deposition methods of graphene as electrode material for organic solar cells, Adv. Energy Mater. 7 (2016) 1601393.
[2] K.S. Novoselov, A.K. Geim, S.V. Morozov, D. Jiang, Y. Zhang, S.V. Dubonos, I.V. Grigorieva, A.A. Firsov, Electric field effect in atomically thin carbon films, Science 306 (5696) (2004) 666–669.
[3] K.S. Novoselov, A.K. Geim, S.V. Morozov, D. Jiang, M.I. Katsnelson, I.V. Grigorieva, S.V. Dubonos, A.A. Firsov, Two-dimensional gas of massless Dirac fermions in graphene, Nature 438 (7065) (2005) 197–200.
[4] A.K. Geim, K.S. Novoselov, The rise of graphene, Nat. Mater. 6 (3) (2007) 183–191.
[5] R. Garg, N. Dutta, N. Choudhury, Work function engineering of graphene, Nanomaterials 4 (2) (2014) 267.
[6] D. Lee, G.D. Kwon, J.H. Kim, E. Moyen, Y.H. Lee, S. Baik, D. Pribat, Significant enhancement of the electrical transport properties of graphene films by controlling the surface roughness of Cu foils before and during chemical vapor deposition, Nanoscale 6 (21) (2014) 12943–12951.
[7] W. Gao, Graphene Oxide: Reduction Recipes, Spectroscopy, and Applications, Springer International Publishing, Cham, 2015.
[8] J. Güttinger, F. Molitor, C. Stampfer, S. Schnez, A. Jacobsen, S. Dröscher, T. Ihn, K. Ensslin, Transport through graphene quantum dots, Rep. Prog. Phys. 75 (12) (2012) 126502.
[9] S. Chen, X. Yu, M. Zhang, J. Cao, Y. Li, L. Ding, G. Shi, A graphene oxide/oxygen deficient molybdenum oxide nanosheet bilayer as a hole transport layer for efficient polymer solar cells, J. Mater. Chem. 3 (36) (2015) 18380–18383.
[10] P. Cheng, Y. Li, X. Zhan, Efficient ternary blend polymer solar cells with indene-C60 bisadduct as an electron-cascade acceptor, Energy Environ. Sci. 7 (6) (2014) 2005–2011.
[11] D. Gedefaw, M. Tessarolo, M. Bolognesi, M. Prosa, R. Kroon, W. Zhuang, P. Henriksson, K. Bini, E. Wang, M. Muccini, M. Seri, M.R. Andersson, Synthesis and characterization of benzodithiophene and benzotriazole-based polymers for photovoltaic applications, Beilstein J. Org. Chem. 12 (2016) 1629–1637.
[12] F. Zheng, W.-L. Xu, H.-D. Jin, X.-T. Hao, K.P. Ghiggino, Charge transfer from poly(3-hexylthiophene) to graphene oxide and reduced graphene oxide, RSC Adv. 5 (109) (2015) 89515–89520.
[13] I. Jung, D.A. Dikin, R.D. Piner, R.S. Ruoff, Tunable electrical conductivity of individual graphene oxide sheets reduced at “low” temperatures, Nano Lett. 8 (12) (2008) 4283–4287.
[14] S. Bai, X. Shen, G. Zhu, Z. Xu, Y. Liu, Reversible phase transfer of graphene oxide and its use in the synthesis of graphene-based hybrid materials, Carbon 49 (13) (2011) 4563–4570.
[15] X. Gao, J. Jang, S. Nagase, Hydrazine and thermal reduction of graphene oxide: reaction mechanisms, product structures, and reaction design, J. Phys. Chem. C 114 (2) (2010) 832–842.
[16] M.A. Velasco-Soto, S.A. Pérez-García, J. Alvarez-Quintana, Y. Cao, L. Nyborg, L. Licea-Jiménez, Selective band gap manipulation of graphene oxide by its reduction with mild reagents, Carbon 93 (2015) 967–973.
[17] Z.J. Li, B.C. Yang, S.R. Zhang, C.M. Zhao, Graphene oxide with improved electrical conductivity for supercapacitor electrodes, Appl. Surf. Sci. 258 (8) (2012) 3726–3731.
[18] M.J. Fernández-Merino, J.I. Paredes, S. Villar-Rodil, L. Guardia, P. Solís-Fernández, D. Salinas-Torres, D. Cazorla-Amorós, E. Morallón, A. Martínez-Alonso, J.M.D. Tascón, Investigating the influence of surfactants on the stabilization of aqueous reduced graphene oxide dispersions and the characteristics of their composite films, Carbon 50 (9) (2012) 3184–3194.
[19] D.R. Dreyer, S. Park, C.W. Bielawski, R.S. Ruoff, The chemistry of graphene oxide, Chem. Soc. Rev. 39 (1) (2010) 228–240.
[20] M. Bernardi, J. Lohrman, P.V. Kumar, A. Kirkeminde, N. Ferralis, J.C. Grossman, S. Ren, Nanocarbon-based photovoltaics, ACS Nano 6 (10) (2012) 8896–8903.
[21] Y.-J. Jeon, J.-M. Yun, D.-Y. Kim, S.-I. Na, S.-S. Kim, High-performance polymer solar cells with moderately reduced graphene oxide as an efficient hole transporting layer, Sol. Energy Mater. Sol. Cell. 105 (2012) 96–102.
[22] S. Qu, M. Li, L. Xie, X. Huang, J. Yang, N. Wang, S. Yang, Noncovalent functionalization of graphene attaching [6,6]-Phenyl-C61-butyric acid methyl ester (PCBM) and application as electron extraction layer of polymer solar cells, ACS Nano 7 (5) (2013) 4070–4081.
[23] P. Robaeys, F. Bonaccorso, E. Bourgeois, apos, J. Haen, W. Dierckx, W. Dexters, D. Spoltore, J. Drijkoningen, J. Liesenborgs, A. Lombardo, A.C. Ferrari, F. Van Reeth, K. Haenen, J.V. Manca, M. Nesladek, Enhanced performance of polymer: fullerene bulk heterojunction solar cells upon graphene addition, Appl. Phys. Lett. 105 (8) (2014), 083306.
[24] J. Wang, Y. Wang, D. He, Z. Liu, H. Wu, H. Wang, Y. Zhao, H. Zhang, B. Yang, Composition and annealing effects in solution-processable functionalized graphene oxide/P3HT based solar cells, Synth. Met. 160 (23–24) (2010) 2494–2500.
[25] Z. Wang, C.P. Puls, N.E. Staley, Y. Zhang, A. Todd, J. Xu, C.A. Howsare, M.J. Hollander, J.A. Robinson, Y. Liu, Technology ready use of single layer graphene as a transparent electrode for hybrid photovoltaic devices, Physica 44 (2) (2011) 521–524.
[26] K.R. Catchpole, A. Polman, Plasmonic solar cells, Optic Express 16 (26) (2008) 21793–21800.
[27] M.-K. Chuang, S.-W. Lin, F.-C. Chen, C.-W. Chu, C.-S. Hsu, Gold nanoparticle-decorated graphene oxides for plasmonic-enhanced polymer photovoltaic devices, Nanoscale 6 (3) (2014) 1573–1579.
[28] C.F. Ou, The effect of graphene/Ag nanoparticles addition on the performances of organic solar cells, J. Mater. Sci. Chem. Eng. 3 (2015) 30–35.
[29] P. Sutradhar, M. Saha, Silver nanoparticles: synthesis and its nanocomposites for heterojunction polymer solar cells, J. Phys. Chem. C 120 (16) (2016) 8941–8949.
[30] W.S. Hummers, R.E. Offeman, Preparation of graphitic oxide, J. Am. Chem. Soc. 80 (6) (1958), 1339-1339.
[31] M.A. Velasco-Soto, S.A. Pérez-García, R. Rychwalski, L. Licea-Jiménez, Chapter 7 - dispersion of carbon nanomaterials A2 - domínguez, in: M. Sánchez, C.R. Abreu (Eds.), Nanocolloids, Elsevier, Amsterdam, 2016, pp. 247–263.
[32] U.A. Méndez-Romero, M.Á. Velasco-Soto, L. Licea-Jiménez, J. Álvarez-Quintana, S.A. Pérez-García, Graphene derivatives: controlled properties, nanocomposites, and energy harvesting applications, in: G.Z. Kyzas, A.C. Mitropoulos (Eds.), Graphene Materials - Structure, Properties and Modifications, InTech, Rijeka, 2017. Ch. 04.
[33] T. Shimanouchi, Tables of molecular vibrational frequencies. Consolidated volume II, J. Phys. Chem. Ref. Data 6 (3) (1977) 993–1102.
[34] J.U. Lee, W. Lee, J.W. Yi, S.S. Yoon, S.B. Lee, B.M. Jung, B.S. Kim, J.H. Byun, Preparation of highly stacked graphene papers via site-selective functionalization of graphene oxide, J. Mater. Chem. 1 (41) (2013) 12893–12899.
[35] D.C. Marcano, D.V. Kosynkin, J.M. Berlin, A. Sinitskii, Z. Sun, A. Slesarev, L.B. Alemany, W. Lu, J.M. Tour, Improved synthesis of graphene oxide, ACS Nano 4 (8) (2010) 4806–4814.
[36] E. Pretsch, P. Bühlmann, M. Badertscher, Summary Tables, Structure Determination of Organic Compounds: Tables of Spectral Data, Springer Berlin Heidelberg, Berlin, Heidelberg, 2009, pp. 1–43.
[37] J. Dong, C. Yin, X. Zhao, Y. Li, Q. Zhang, High strength polyimide fibers with functionalized graphene, Polymer 54 (23) (2013) 6415–6424.
[38] W.-S. Hung, C.-H. Tsou, M. De Guzman, Q.-F. An, Y.-L. Liu, Y.-M. Zhang, C.-C. Hu, K.-R. Lee, J.-Y. Lai, Cross-linking with diamine monomers to prepare composite graphene oxide-framework membranes with varying d-spacing, Chem. Mater. 26 (9) (2014) 2983–2990.
[39] M. Acik, G. Lee, C. Mattevi, M. Chhowalla, K. Cho, Y.J. Chabal, Unusual infrared-absorption mechanism in thermally reduced graphene oxide, Nat. Mater. 9 (10) (2010) 840–845.
[40] C.K. Chua, M. Pumera, Light and atmosphere affect the quasi-equilibrium states of graphite oxide and graphene oxide powders, Small 11 (11) (2015) 1266–1272.
[41] Y. Li, X. Pei, B. Shen, W. Zhai, L. Zhang, W. Zheng, Polyimide/graphene composite foam sheets with ultrahigh thermostability for electromagnetic interference shielding, RSC Adv. 5 (31) (2015) 24342–24351.
[42] P.V. Kumar, N.M. Bardhan, S. Tongay, J. Wu, A.M. Belcher, J.C. Grossman, Scalable enhancement of graphene oxide properties by thermally driven phase transformation, Nat. Chem. 6 (2) (2014) 151–158.
[43] T. Carey, S. Cacovich, G. Divitini, J. Ren, A. Mansouri, J.M. Kim, C. Wang, C. Ducati, R. Sordan, F. Torrisi, Fully inkjet-printed two-dimensional material field-effect heterojunctions for wearable and textile electronics, Nat. Commun. 8 (1) (2017) 1202.
[44] D.A. Burns, E.W. Ciurczak, Handbook of Near-Infrared Analysis, CRC press, 2007.
[45] A. Mathkar, D. Tozier, P. Cox, P. Ong, C. Galande, K. Balakrishnan, A. Leela Mohana Reddy, P.M. Ajayan, Controlled, stepwise reduction and band gap manipulation of graphene oxide, J. Phys. Chem. Lett. 3 (8) (2012) 986–991.
[46] R. Su, S.F. Lin, D.Q. Chen, G.H. Chen, Study on the absorption coefficient of reduced graphene oxide dispersion, J. Phys. Chem. C 118 (23) (2014) 12520–12525.
[47] Y.T. Liang, M.C. Hersam, Highly concentrated graphene solutions via polymer

enhanced solvent exfoliation and iterative solvent exchange, J. Am. Chem. Soc. 132 (50) (2010) 17661–17663.
[48] M.M. Stylianakis, M. Sygletou, K. Savva, G. Kakavelakis, E. Kymakis, E. Stratakis, Photochemical synthesis of solution-processable graphene derivatives with tunable bandgaps for organic solar cells, Adv. Optical Mater. 3 (5) (2014) 658–666.
[49] M.C. Scharber, N.S. Sariciftci, Efficiency of bulk-heterojunction organic solar cells, Prog. Polym. Sci. 38 (12) (2013) 1929–1940.
[50] W. Shockley, H.J. Queisser, Detailed balance limit of efficiency of p-n junction solar cells, J. Appl. Phys. 32 (3) (1961) 510–519.
[51] M. Young, J. Suddard-Bangsund, T.J. Patrick, N. Pajares, C.J. Traverse, M.C. Barr, S.Y. Lunt, R.R. Lunt, Organic heptamethine salts for photovoltaics and detectors with near-infrared photoresponse up to 1600 nm, Adv. Optical Mater. 4 (7) (2016) 1028–1033.
[52] A. Moliton, J.-M. Nunzi, How to model the behaviour of organic photovoltaic cells, Polym. Int. 55 (6) (2006) 583–600.
[53] M. Obiols-Rabasa, Chapter 9 - non-invasive characterization methods for nanocolloids A2 - domínguez, in: M. Sánchez, C.R. Abreu (Eds.), Nanocolloids, Elsevier, Amsterdam, 2016, pp. 299–330.
[54] R.L.D. Whitby, A. Korobeinyk, V.M. Gun'ko, R. Busquets, A.B. Cundy, K. Laszlo, J. Skubiszewska-Zieba, R. Leboda, E. Tombacz, I.Y. Toth, K. Kovacs, S.V. Mikhalovsky, pH-driven physicochemical conformational changes of single-layer graphene oxide, Chem. Commun. 47 (34) (2011) 9645–9647.
[55] R.L.D. Whitby, V.M. Gun'ko, A. Korobeinyk, R. Busquets, A.B. Cundy, K. László, J. Skubiszewska-Zięba, R. Leboda, E. Tombácz, I.Y. Toth, K. Kovacs, S.V. Mikhalovsky, Driving forces of conformational changes in single-layer graphene oxide, ACS Nano 6 (5) (2012) 3967–3973.
[56] C.D. Zangmeister, X. Ma, M.R. Zachariah, Restructuring of graphene oxide sheets into monodisperse nanospheres, Chem. Mater. 24 (13) (2012) 2554–2557.